AGU PUBLICATIONS

JGR

Journal of Geophysical Research: Space Physics

RESEARCH ARTICLE
10.1002/2016JA022965

Special Section:
Geospace system responses to the St. Patrick's Day storms in 2013 and 2015

Small-scale structure of the midlatitude storm enhanced density plume during the 17 March 2015 St. Patrick's Day storm

Thomas R. P. Heine[1], Mark B. Moldwin[1], and Shasha Zou[1]

[1]Department of Climate and Space Sciences and Engineering, University of Michigan, Ann Arbor, Michigan, USA

Key Points:
- Kilometer-scale density irregularities measured in single-station GPS TEC data from the 17 March 2015 storm enhanced density plume system
- Location, intensity, and length scales are estimated from spatial, temporal, and frequency analyses of multiple instrument data
- Formation regions for small-scale irregularities with length scales of 3-10 km are identified for plasma velocities of 500–1200 m s^{-1}

Supporting Information:
- Movie S1

Correspondence to:
T. R. P. Heine,
heinet@umich.edu

Citation:
Heine, T. R. P., M. B. Moldwin, and S. Zou (2017), Small-scale structure of the midlatitude storm enhanced density plume during the 17 March 2015 St. Patrick's Day storm, *J. Geophys. Res. Space Physics*, *122*, 3665–3677, doi:10.1002/2016JA022965.

Received 18 MAY 2016
Accepted 24 JAN 2017
Accepted article online 31 JAN 2017
Published online 20 MAR 2017

Abstract Kilometer-scale density irregularities in the ionosphere can cause ionospheric scintillation—a phenomenon that degrades space-based navigation and communication signals. During strong geomagnetic storms, the midlatitude ionosphere is primed to produce these ~1–10 km small-scale irregularities along the steep gradients between midlatitude storm enhanced density (SED) plumes and the adjacent low-density trough. The length scales of irregularities on the order of 1–10 km are determined from a combination of spatial, temporal, and frequency analyses using single-station ground-based Global Positioning System total electron content (TEC) combined with radar plasma velocity measurements. Kilometer-scale irregularities are detected along the boundaries of the SED plume and depleted density trough during the 17 March 2015 geomagnetic storm, but not equatorward of the plume or within the plume itself. Analysis using the fast Fourier transform of high-pass filtered slant TEC suggests that the kilometer-scale irregularities formed near the poleward gradients of SED plumes can have similar intensity and length scales to those typically found in the aurora but are shown to be distinct phenomena in spacecraft electron precipitation measurements.

1. Introduction

The small-scale (~1–10 km) density structure of the storm time, midlatitude ionosphere is a crucial observation in understanding the space weather effects on key space-based infrastructure and especially communication and navigation systems. Though these systems are generally unaffected by the midlatitude ionosphere, there can be significant technological impacts during strong geomagnetic storms. Geomagnetic storms have been shown to drive structural changes in the Earth's ionosphere that deviate dramatically from the typical quiet time conditions [e.g., *Foster and Rideout*, 2005] and observations of total electron content (TEC) have revealed that some of the most dramatic changes are the storm enhanced density (SED) plumes that occur in the midlatitude ionosphere [e.g., *Foster*, 1993; *Kelley et al.*, 2004; *Zou et al.*, 2013, 2014]. Storm enhanced density (SED) plumes and the subauroral polarization stream (SAPS) can generate radio-disrupting ionospheric density irregularities [*Foster and Burke*, 2002; *Basu et al.*, 2008] that produce up to 20 dB signal fade at the Global Positioning System (GPS) L1 (1575 MHz) frequency and scintillations in HF and VHF communications [*Basu and Groves*, 2001; *Ledvina et al.*, 2002; *Seo et al.*, 2011]. Steep density gradients along the plumes' edges can produce a cascade of small-scale density irregularities and subsequently, a potentially worsening scintillation environment for Global Navigation Satellite Systems (GNSS) such as GPS and space-based communication users. Small-scale variations (or irregularities) in ionospheric electron density corresponding to the Fresnel radius of radio frequencies—between 100 MHz and 3 GHz for a receiver on the ground—can dramatically impact space-based systems operating in this frequency range [*Datta-Barua et al.*, 2014; *Doherty et al.*, 2004; *Datta-Barua et al.*, 2003].

This paper will demonstrate, through a case study of the 17 March 2015 geomagnetic storm, a proof of concept for the detection and characterization of small-scale (~1 – 10 km) density irregularities from a single GPS TEC station (located in Ann Arbor, Michigan— 42.29°N, −83.71°E Geodetic, 53.31°N, −10.34°E CGM). When the single station TEC data is combined with coherent high frequency (HF) and incoherent scatter radar (ISR) plasma velocities, the length scale of irregularities is inferred. Further, by the overlaying the location of the single station TEC measurements on publicly available TEC maps from the MIT Madrigal Archival Database, observations of irregularities are illustrated in the context of the broader SED plume background system.

These are the first observations of midlatitude kilometer-scale irregularities during a SED event to identify length scales from single-station GPS TEC.

1.1. Background

The origins of kilometer-scale irregularities at midlatitudes owe to three potential sources. In the first, spatially structured and temporally variable particle precipitation produces localized small-scale structure in the *E* and *F* regions of the auroral zone. [*Schunk and Nagy*, 2009]. In the second, it has been suggested that small-scale irregularities are generated near the SED plume by a horizontal Rayleigh-Taylor instability (also known as the gradient drift instability) caused by the motion of lower density plasma moving into the density gradient. This condition becomes unstable when $(\mathbf{E} \times \mathbf{B}) \cdot \nabla n > 0$ [*Simon*, 1963; *Sun et al.*, 2013]. Finally, in the third, velocity shear instability (Kelvin-Helmholtz) may play a role in generating small-scale irregularities at the interface between fluids of different densities [*Hargreaves*, 1992], such as in the case of the SED/SAPS boundary. Although the physics underpinning the formation of small-scale irregularities is well understood, the complexity of the storm time midlatitude ionosphere demands further observation and characterization of its density structure at all scales to improve our understanding of the typical formation and evolution of storm time small-scale irregularities and the potential for midlatitude radio scintillation. This paper describes a method for detecting small-scale density irregularities using spectral analysis (fast Fourier transform) of GPS TEC observations from a single ground station while simultaneously "zooming-out" to see the location of the single station measurements in the broader (1000 km) context of the SED plume system.

Midlatitude irregularities and scintillation have been a subject of study for several decades. An early investigation by *Bramley and Browning* [1978], over a 12 month period, analyzed the spectral composition of VHF scintillation near Slough, in Berkshire, England, using spaced, antennas to measure amplitude fluctuations from the interaction between a geostationary satellite signal and ionospheric irregularities. They were able to infer both the irregularity size and approximate orientation from the ground diffraction pattern. The irregularities they observed had characteristic spatial scales ranging from 180 m to 2 km and found no correlation of the occurrence of these irregularities with geomagnetic activity—suggesting their observations were not of storm related effects.

The storm time effects of SED have been extensively described in the literature over the past decade. *Doherty et al.* [2004] established a connection between SED gradients and disruption of the Federal Aviation Administration's Wide-Area Augmentation System (WAAS) during the October/November 2003 "Halloween Storms." During those events, the WAAS vertical navigation system was inoperable for more than 28 h over a 2 day period. Similarly, *Basu et al.* [2008] looked at a geomagnetic storm 7–8 November 2004 with a minimum Kyoto disturbance storm time index (*Dst*) of −394 nT. They observed midlatitude GNSS disruption due to irregularities from an expanding auroral oval and nighttime subauroral polarization stream (SAPS) flow. *Datta-Barua et al.* [2014] also described the impact on the WAAS during 24–25 October 2011 and 9 October 2012 geomagnetic storms that included reduced service coverage over the continental United States lasting several hours and anomalous receiver tracking due to ionospheric scintillation.

Coster [2007] first reported the impact of small-scale TEC variability on the performance of key infrastructure, including WAAS, and specifically the impact of TEC gradients. Using observations of GPS tracks crossing SED plumes, *Coster* [2007] observed that the TEC gradients near SED plumes can exhibit differing degrees of variability and even between the poleward and equatorward gradients. The nature and specific irregularity length scales of such crossings remain an open research area.

Another study by *Sun et al.* [2013] analyzed the formation of irregularities associated with North American SED plumes during geomagnetic storms on 31 March 2001 (*Dst* = −387 nT) and 30 October 2003 (*Dst* = −383 nT). In their study, the presence of irregularities was indicated in TEC maps with 0.5° × 1.0° resolution using a 30 s rate of TEC (ROT) and the ROT index (ROTI) formulated by *Pi et al.* [1997] at each grid point. ROT and ROTI are defined as the differential vertical TEC (VTEC) between time steps converted to TEC units per minute (TECU/min), where a TECU = 1×10^{16} electrons m^{-2}, and the standard deviation of the ROT over a specified time interval—commonly 5 min. *Sun et al.* [2013] observed that irregularities were most present along the poleward boundary of the SED—along the low-density trough—and that the irregularity intensity increased with steepening TEC gradients in some cases. They concluded that the formation of irregularities appeared to depend on both steep TEC gradients and strong ion drifts (1–2 km s^{-1}) as favorable conditions. However, while they identified the presence of irregularities and the gradients associated with ROTI, they did not specify the length scale of irregularities present in each grid cell.

Previously, characteristic sizes of midlatitude small-scale irregularities associated with SED plumes have been inferred from amplitude scintillation measurements at a fixed point [*Basu et al.*, 2008], and *van der Meeren et al.* [2014] used similar methodology to that presented here to identify irregularities in 50 Hz GPS phase data detrended with fourth-order polynomial fit and a high-pass Butterworth filter to investigate irregularities at the front of a polar tongue of ionization on 31 October 2011. They found phase variations at spatial scales from 100 m to 5 km using spectrograms and estimates of TOI drift speed from arrival time of the tongue of ionization at two European Incoherent Scatter radar antennae.

To date, there have been no such studies inferring the spatial scale of kilometer-scale irregularities associated with midlatitude SED plumes from single station GPS TEC using multiple GPS tracks through an SED plume system. This paper describes the detection and length-scale estimation of irregularities associated with the midlatitude SED plume as it moves over the GPS receiver during the 17 March 2015 geomagnetic storm.

1.2. The 2015 St. Patrick's Day Storm

On 17 March 2015, the Earth experienced a G4 "severe" geomagnetic storm on the National Oceanic and Atmospheric Administration (NOAA) geomagnetic storm scale (Love and Rigler, 2015, https://geomag.usgs.gov/storm/storm22.php, 26 May 2015). At 04:45 UTC, the Kyoto *Dst* indicated a 55 nT enhancement of the horizontal geomagnetic field which is characteristic of a sudden storm commencement. The storm reached the peak of its main phase around 19:00 UTC with minimum magnetic field disturbances: Kyoto Provisional $Dst = -223$ nT and $SYM\text{-}H = -234$ nT. Over the period between 16 March 2015 and 19 March 2015, the planetary *K* index (*Kp*) was greater than 5 for 48 of 72 h and $Kp = 8$ for a total of 9 h during the main phase of the storm. Meanwhile, throughout 17 and 18 March, the *K* index reached $Kp \geq 7$ on 4 of twenty-four 3 h periods and above 5 during 16 periods. A SED plume was observed in the Massachusetts Institute of Technology (MIT) Madrigal TEC map during the North American afternoon/dusk period on 17 March (shown in Figure 1). The SED plume began in a region of enhanced TEC (the SED base) that was poleward and distinct from the TEC peaks of the enhanced equatorial anomaly. The plume extended to the northwest across the Great Lakes region and toward the noontime cusp. A low-density, midlatitude trough is also visible in Figure 1, while the auroral oval extended as far south as 39° geographic latitude at 23:17 UT (inferred from Figure 6 and discussed in section 3.5). The *Dst* minimum was reached at approximately 23:00 UT. This paper includes observations from a single GPS station in Ann Arbor, Michigan: ANNA (42.29°N, −83.71°E Geodetic; 53.31°N, −10.34°E CGM) during the end of the main phase and the beginning of the recovery phase between 20:00 UT 17 March 2015 and 23:57 UT 18 March 2015. The availability of high-rate (1 Hz) TEC is rare within this region for this time. Of the few stations within 250 km of Ann Arbor that have 1 Hz data available during this event, two Canadian stations, ALGO (45.96° N −78.07° E GEO, 56.74° N −2.57° E CGM) and NRC1 (45.454° N −75.62° E GEO, 56.04° N 0.97° E CGM), do have 1 Hz data for this time but are too high in latitude and too far ahead in local time relative to the SED plume to distinguish between auroral precipitation and plume generated irregularities and are therefore not used. Within 1000 km, there are six stations in the UNAVCO database with 1 Hz data rates. Stations in Ames, IA (AMES: 41.98° N −93.68° E GEO, 52.58° N −25.37° E CGM) and near St. Clairsville, PA (P817: 40.14°N −78.51°E GEO, 52.59° N −3.51°E CGM) were analyzed using the same methods described in section 2 of this paper and produce similar results to the data observed at ANNA in terms of general trend, but being 900 km west and 700 km east of ANNA, respectively, they exhibit the expected localized differences in density structure >10 km. This suggests that for the purpose of this study, ANNA is representative of the available 1 Hz GPS TEC data for this event.

2. Methodology

Kilometer-scale irregularities are identified near the SED plume using multiple line-of-sight GPS TEC measurements from a single GPS receiver. Slant TEC (STEC) from each GPS satellite/receiver pair was measured at 1 Hz using a Trimble NetR9 dual-frequency GPS receiver, and pseudorandom noise (PRN) codes—assigned 1–32 to each of the currently operational GPS spacecraft—are used to identify individual satellites and their associated Ionospheric Pierce Points (IPP). IPPs are defined as the point of intersection between a GPS signal path and the altitude of the ionospheric *F* peak, which is approximated as a spherical shell at 300 km altitude. TEC is derived from the differential (GPS L1 and L2 frequencies) P-code pseudorange and the carrier phase. The two-frequency differential carrier phase measurement allows precise measurement of the carrier phase delay while the PRN code pseudorange is used to resolve the cycle ambiguity inherent to the carrier phase measurements. The STEC is converted to the local vertical TEC (VTEC) at the IPP using a spherical mapping function.

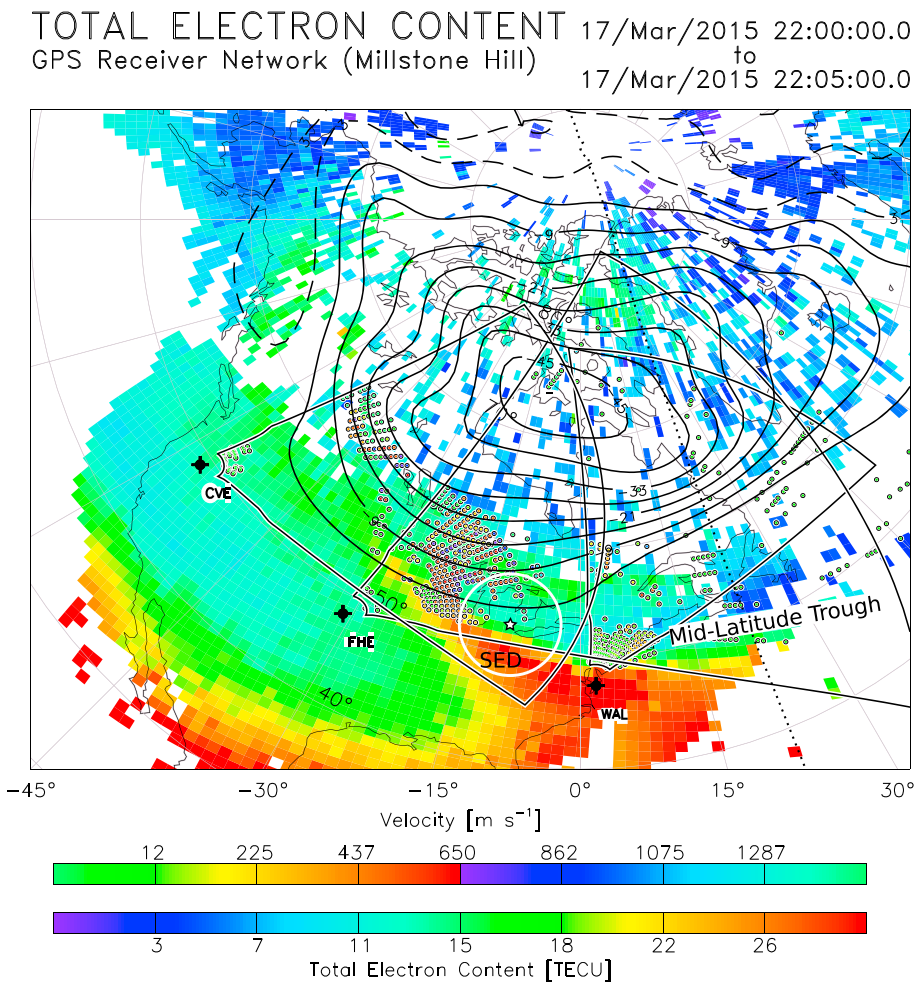

Figure 1. The SED plume is visible in the 1° × 1° TEC map as a red band stretching toward the northwest at 22:00 UT. The colored circles indicate the location of SuperDARN radar backscatter and line-of-sight plasma speeds from Christmas Valley East, Fort Hays East, and Wallops Island, while the polar equipotential lines (solid lines) show the direction of plasma convection (westward within the Great Lakes region). The day/night terminator is shown as a dotted line. *Figure courtesy of Evan Thomas, Virginia Technological University.*

A postprocessing elevation mask of 20° is applied to reduce errors from the vertical mapping function and obstructions near the horizon.

The STEC data are then filtered using a tenth-order Butterworth high-pass filter shaped with stop and pass frequencies at 30 and 100 mHz, respectively. The filter's frequency and forward phase response are shown in Figure 2 (top). The filter is designed to suppress the low-frequency background density structure in STEC while maintaining higher-frequency power from smaller fluctuations. It is also designed to minimize phase shifts, and the filter function was convolved with the data both forward and backward to further cancel phase changes to the filtered signal. The unfiltered and filtered STEC are shown in Figure 2 (bottom).

The discrete (fast) Fourier transform (FFT) of the filtered STEC for each PRN was computed in a sliding 5 min window advanced in 10 s increments. The sliding 5 min window (300 samples, 290 overlap) was chosen as a balance between three factors: first, to achieve a sufficient number of samples to resolve spectra with a resolution of at least 0.1 Hz; second, to maintain a sufficiently short IPP track (~15 km) so that the resulting spectra can be attributed to a specific location within the SED plume system (e.g., a gradient crossing); and third, to take advantage of the maximum temporal resolution available from the TEC maps which are updated every 5 min.

Additionally, to ensure a consistent number of samples between PRN in each FFT interval, measurements of PRN that were visible less than 90% of the interval were excluded from analysis.

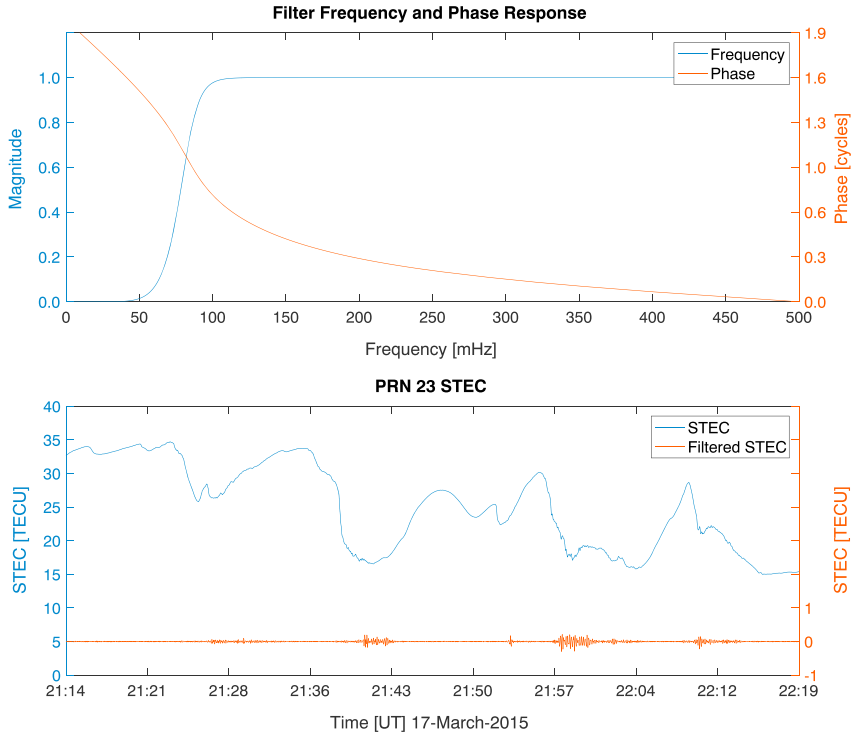

Figure 2. (top) Frequency and phase response of high-pass filter used to remove low-frequency (<100 mHz, long temporal) background from the STEC signal. (bottom) The unfiltered STEC signal from PRN 23 is shown in blue, while the filtered signal is shown in orange. The filter removed the large-scale STEC variations associated with the SED plume in order to extract smaller-scale variations of interest to this study.

Finally, by combining the FFT spectra with the radar velocity measurements, including those shown in Figure 1, the length scales of small-scale variability can be estimated. Millstone Hill radar measures the plasma drift velocity during azimuthal scans looking at 6° elevation toward the west and observes the ionosphere at a height of ~300 km above the Ann Arbor viewing area. Several midlatitude SuperDARN radars (Blackstone, Christmas Valley East, Fort Hays East, and Wallops Island) also measure plasma velocity in this region. If it is assumed that irregularities are frozen-in with the background plasma flow (as has been suggested by, e.g., *Yeh and Liu* [1982] and the IPP velocity $v_{ipp} \ll v_{ion}$, (v_{ipp} ~50 m s^{-1}), then the FFT power at various frequencies can reasonably be attributed to irregularities of certain length scales being transported past the relatively stationary IPP at the plasma velocity. Consider the simplified scenario: discrete and uniformly spaced boxcar irregularities passing a nearly stationary IPP produce a periodicity in the slant TEC data that is revealed in the FFT frequency domain. Therefore, if the irregularity velocity is known (which is assumed to be with the background plasma velocity), then the irregularity length-scale can be estimated by $L_{irr} \approx v_{ion}/f_{FFT}$. Uncertainty introduced by the IPP velocity contributes only at most a shift in the frequency spectra of ~0.005 Hz within the 0–0.5 Hz Nyquist window.

Unlike methods that measure signal amplitude to detect ionospheric variability and scintillation at the signal frequency, this method can be used to detect irregularities of multiple length scales and is limited only by the TEC sample rate. The case presented here uses TEC sampled at 1 Hz. Future studies will extend this approach to sample rates of 20 Hz and higher to include smaller length scales and expand to include multiple GPS TEC stations.

The single station TEC measurements and analysis are compared and contextualized in the broader SED plume system using multistation GPS TEC maps downloaded from the MIT Madrigal archival site at Millstone Hill, MA. The location of the Ann Arbor station IPP tracks are then superimposed on the MIT Madrigal TEC map. The MIT Madrigal Database provides global maps of TEC on a 1°×1° spatial grid updated every 5 min. The maps are fitted to a 1/6°×1/6° subgrid mesh using bicubic spline interpolation—a common image sharpening technique. The interpolated map clarifies the locations and boundaries of the SED plume, depleted density trough and auroral enhancement region so that the location of the IPPs from the single-station data can be plotted on the

map and categorized by their location within the SED plume system. However, since interpolation cannot add information, the location of structural dimensions appearing less than a degree in scale, such as the plume boundary's thickness, is uncertain using the TEC map data alone; however, TEC structures with dimensions larger than a degree (e.g., the line of the plume boundary, 10–20° longitude in length) are reliably defined using this technique. Definitive boundary crossings of each IPP are confirmed using the direct measurement Ann Arbor single station TEC time series.

While the Madrigal TEC maps provide the background density structure with spatial scales on the order of the SED plume system (100–1000 km) at a cadence of 5 min, the Ann Arbor STEC data provide measurements of the density structure on much smaller (<100 km) spatial and temporal scales. GPS IPP tracks for the Ann Arbor receiver are calculated from the precise GPS satellite ephemeris, provided by the International GNSS Service and the NASA Jet Propulsion Laboratory in Standard Product-3 (.SP3) format, and are superimposed onto the TEC maps to illustrate where the small-scale STEC measurements were made relative to the background SED plume density structure.

One of the interesting, and perhaps counterintuitive, aspects of the Earth-fixed TEC maps is the apparent southwestward motion of the SED plume through the observation area. This is due to two factors.

1. At midlatitudes, the SED plume is connected to the plasmaspheric convection flow and does not corotate with the Earth. A consequence is, in the Earth-fixed inertial frame, the Earth rotates underneath the plume—giving the impression of a westward moving plume.
2. The plasma within the plume is convecting to the northwest from a broader base region and is angled relative to the Earth's eastward rotation. This means that what appears in figures to be a southward component in the motion of the plume is actually due to the Earth rotating under a broader region of the plume near the SED base region.

An animation (Movie S1) encompassing the period from 20:00 UT to 23:57 UT 17 March 2015 to combine single station VTEC time series, sliding FFT, and MIT Madrigal TEC maps into three panes. Each of the animation's three panes are synchronized with the 5 min TEC map update and IPP track nearest to the start of the FFT epoch. Since the IPP move at about 50 m s^{-1}, a 5 min window covers ~15 km and the IPP tracks appear as short line segments overlaid in the mapping pane. The VTEC time series and FFT are updated more frequently—corresponding to the 10 s sliding FFT window. A gray vertical bar superimposed on the VTEC time series illustrates the period of the FFT interval. Meanwhile, the Madrigal TEC map is updated when the leading edge of the FFT window is at the midpoint between 5 min map update intervals. This ensures that the displayed map best represents the background against which the single station TEC FFT was computed.

In addition to GPS TEC observations, observations from the Defense Meteorological Satellite Program (DMSP) and the Active Magnetosphere and Planetary Electrodynamics Response Experiment (AMPERE) are used to locate regions of auroral precipitation. DMSP measures vertical electron and ion fluxes, while AMPERE estimates the hemispherical polar radial field-aligned current density derived from reduced magnetic field perturbation data from the Iridium satellite constellation. The DMSP and AMPERE observations are used here to estimate the location of the auroral oval's equatorward boundary in order to delineate between the density irregularities and enhancements caused by aurora and those associated with the SED plume.

3. Observations

The SED plume is clearly visible from VTEC data in the observation area beginning around 20:00 UT. Figures 3–6 show results from key intervals, 20:40, 22:00 23:00, and 23:20 UT, during the SED plume's passage over the Ann Arbor observation area. Each of these figures contains (left) the track of IPPs in relation to the SED plume, (right top) the VTEC time series, and (right bottom) the 5 min STEC FFT. Observations for the entire period of 20:00 UT 17 March 2015 to 23:57 UT 17 March 2015 are contained in the supporting information Movie S1.

3.1. 20:00 to 20:45 UT, Entering the SED Plume

During the period from 20:00 to 20:45 UT, the SED plume's equatorward edge and density peak passed over Ann Arbor (Figure 3). Overall, VTEC measurements from PRN IPPs that tracked equatorward of the SED plume were comparable to quiet time levels, and those that tracked near or inside the plume showed VTEC that was elevated above quiet time levels with minimal increased variability seen in the VTEC time series. For example, PRN 3, shown in bright green in Figure 3, has an IPP that remained ahead of the plume's

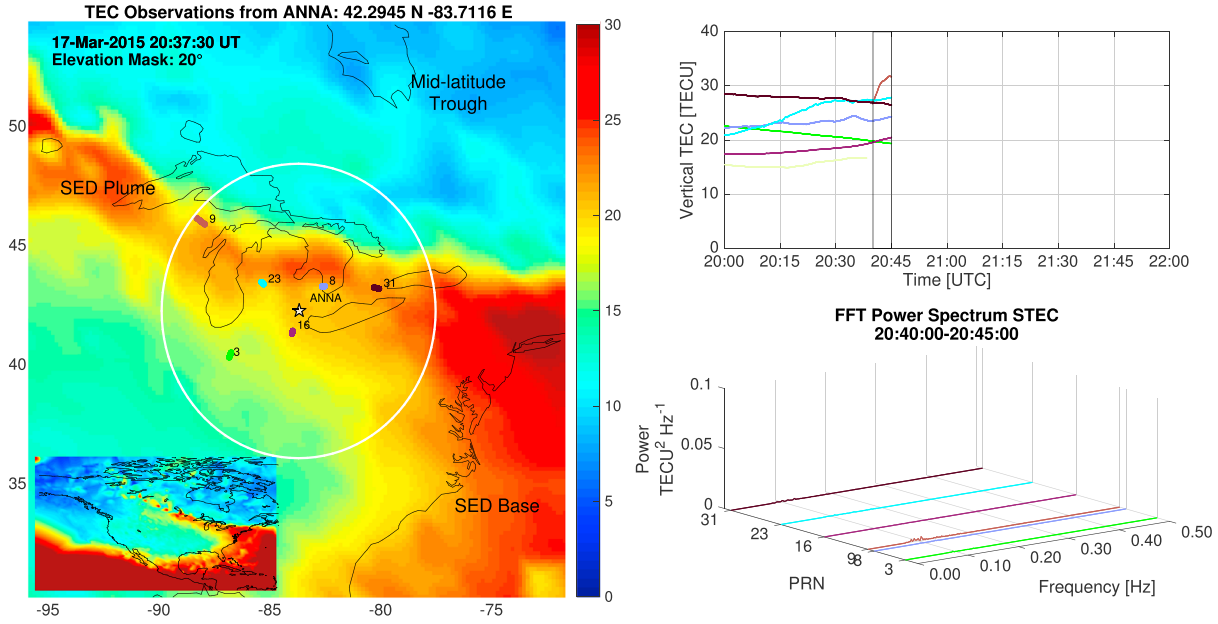

Figure 3. (left) Interpolated Madrigal VTEC map with 5 min IPP tracks for the interval ending at 20:45 UT. The location of the ANNA receiver is marked with a five-pointed star and a white circle demarcates the field-of-view boundary with a 20° elevation mask. The SED plume, SED base region, and midlatitude trough are visible. TEC over North America (inset). (right top) The cumulative VTEC time series from 20:00. The 5 min FFT window is indicated by the two black vertical lines at the end of the time series. (right bottom) The 5 min FFT for the observable GPS PRN.

advancing equatorward edge and showed smooth and relatively constant VTEC values with little FFT power above 100 mHz. By contrast, PRN 16 (purple), which tracked poleward into the plume, showed smooth but increasing VTEC. Around 20:37, as it traveled $>1°$ equatorward of the plume's equatorward edge, PRN 3 exhibited an increase in FFT power just above 100 mHz, though there were no variations observed at other frequencies or the VTEC times series. Also during this time, PRN 23 (light blue) and PRN 31 (black) were observed

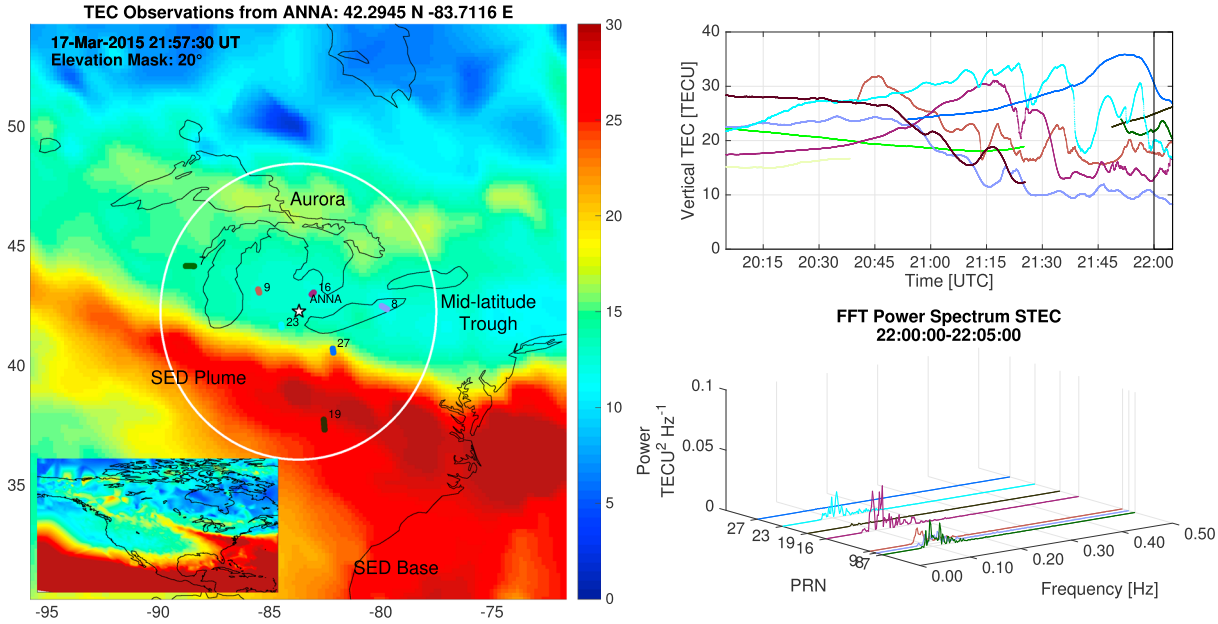

Figure 4. (left) Interpolated Madrigal VTEC map with 5 min IPP tracks for the interval ending at 22:05 UT. The location of the ANNA receiver is marked with a five-pointed star and a white circle demarcates the field-of-view boundary with a 20° elevation mask. The SED base region, SED plume, midlatitude trough, and auroral enhancement are visible from bottom to top. TEC over North America (inset). (right top) The cumulative VTEC time series from 20:00. The 5 min FFT window is indicated by the two black vertical lines at the end of the time series. (right bottom) The 5 min FFT for the observable GPS PRN.

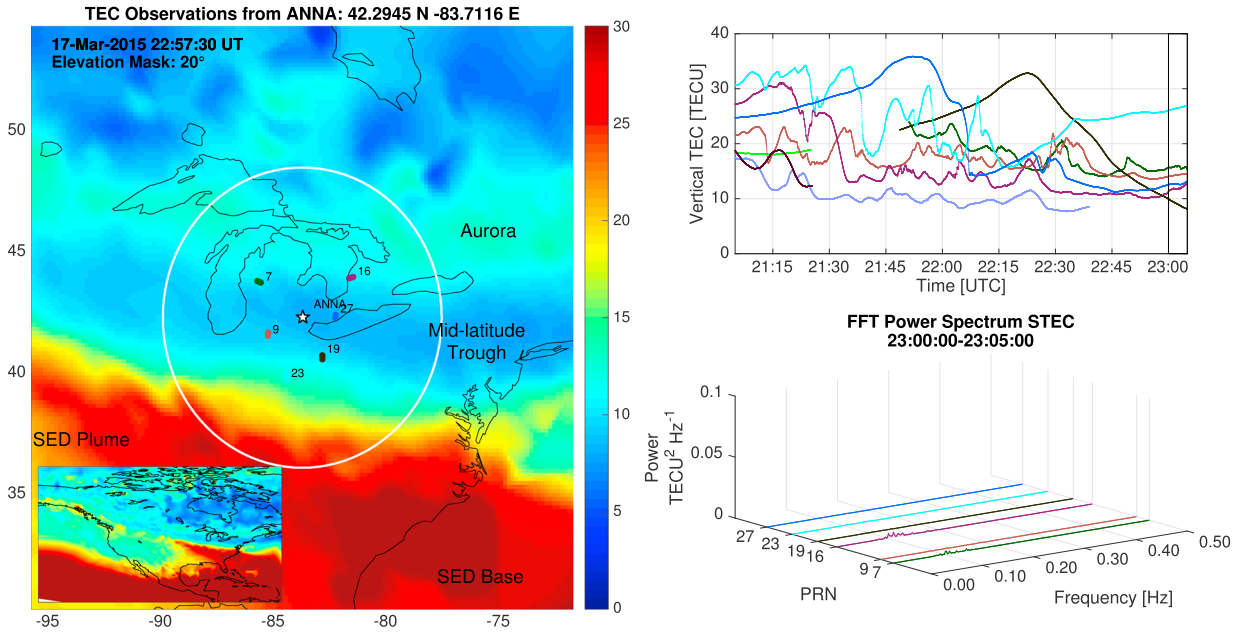

Figure 5. (left) Interpolated Madrigal VTEC map with 5 min IPP tracks for the interval ending at 23:05 UT. The SED base region, SED plume, midlatitude trough, and auroral enhancement are visible from bottom to top with all IPP tracks (with the exception of PRN 23) are located in the midlatitude trough. TEC over North America (inset). (right top) The cumulative VTEC time series from 21:00. (right bottom) The 5 min FFT for the observable GPS PRN.

inside the plume and near its equatorward edge (not shown). PRN 23 was located in a narrower, westward portion of the plume at −86°E, while PRN 31 was located to the east (near −81°E) and closer to the SED base region. Both exhibited elevated VTEC, although PRN 23 was initially ~7 TECU lower than PRN 31. Between 20:00 and 20:45, the plume moved so that both PRNs 23 and 31 were tracking across the plume. PRN 23 VTEC increased steadily, though with persistent small-scale variations and a slight increase in FFT power just

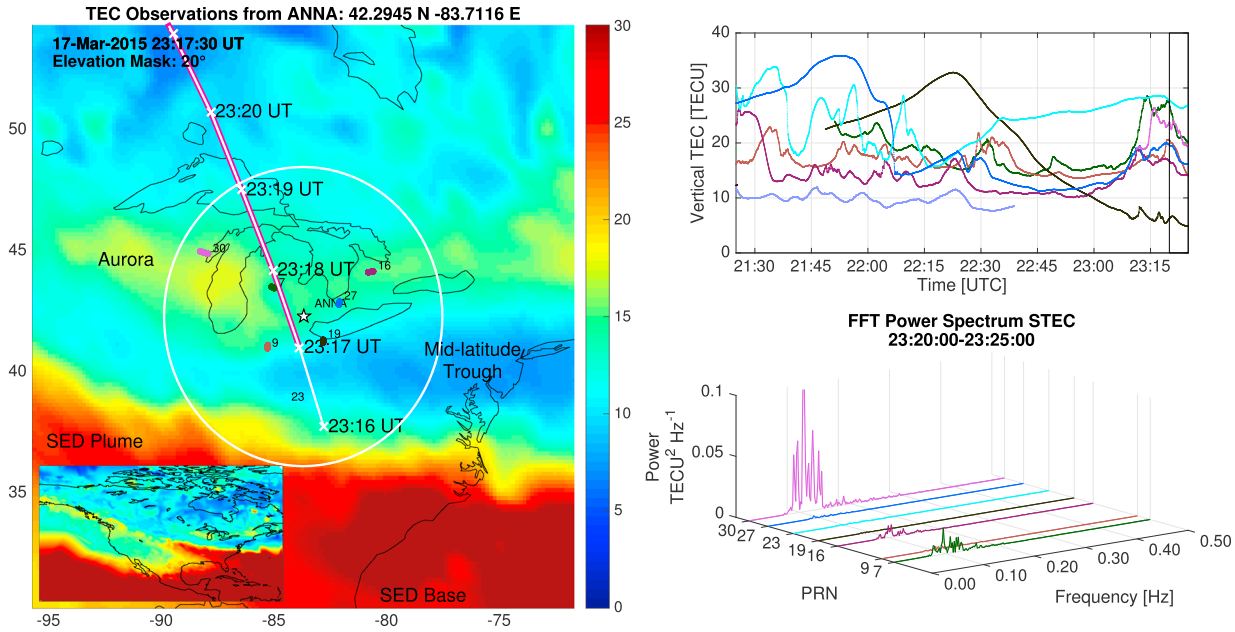

Figure 6. (left) Interpolated Madrigal VTEC map with 5 min IPP tracks for the interval ending at 23:205 UT. The SED plume, SAPS, trough, and auroral enhancement are visible from bottom to top, and all of the IPP tracks (except PRN 23) are located within the auroral zone. The magnetic footprint track for DMSP F17 mapped to 300 km altitude (white line) is also shown with the detected enhanced particle precipitation (shown in Figure 7) flux highlighted in magenta along the track beginning near ~41°N. TEC over North America (inset). (right top) The cumulative VTEC time series from 23:25. (right bottom) The 5 min STEC FFT for the observable GPS PRN.

above the noise floor at ~0.005 TECU^2 Hz^{-1} near 100 mHz at 20:20 UT—corresponding to its crossing into a large-scale bite-out in VTEC along the SED plume's poleward edge. PRN 31 VTEC held at a consistent 26–27 TECU and exhibited small variations in the VTEC time series, but these did not significantly affect the FFT power spectra (<0.005 TECU^2 Hz^{-1}). PRN 31 also tracked between some of the plume's 1–2° longitude high density structures visible in the VTEC map—suggesting a possible explanation for its near constant VTEC.

3.2. 20:45 to 21:20 UT, Longitudinal Asymmetries and Inside the Plume

At 20:45 the plume crossed the PRN 9 IPP, which tracked parallel to the plume's poleward edge. PRN 9 registered an increase of 5 TECU accompanied by a slight increase in FFT power just above 0.005 TECU^2 Hz^{-1} at 100 mHz upon entering the plume before it was again crossed by the plume's poleward edge, when it recorded a drop in VTEC of ~15 TECU and exhibited rapid fluctuations in VTEC of ~3–5 TECU with periods of 5–10 min through the decrease. These decreases were accompanied by FFT power of 0.04 TECU^2 Hz^{-1} between 100 and 300 mHz. PRN 31 was observed along a similar path along the plume's poleward edge, though farther east—near −80°E. VTEC for PRN 31 was 5 TECU less than PRN 9 but registered a comparable decrease in VTEC after crossing the plume's edge. However, in contrast with PRN 19, the decrease exhibited smooth fluctuations over distances of ~30 km, which were accompanied by a broadband increase in FFT power that continued until PRN 31 left the observation area at 21:25 UT. Meanwhile, PRNs 16 and 23 both showed increased VTEC as they moved through the SED plume. PRN 23 initially continued its track inside the plume along its length, from −87° to −85°E and near the poleward edge. It crossed the poleward edge at 21:00, and the arc of its IPP track continued a southward turn that followed behind the plume's advancing poleward edge. This afforded sustained observations of the plume's poleward boundary which exhibited large undulations in VTEC of ~10 TECU over periods of approximately 10 min accompanied by FFT power up to 0.03 TECU^2 Hz^{-1}. PRN 16 continued tracking northward through the plume and toward the poleward edge near −80°E. Instead of small-scale variations observed in PRN 23 as it crossed the plume, PRN 16 exhibited only smooth increases in VTEC with large-scale variations of 1–3 TECU over ~10 km observed, similar to PRN 23, with no observable change in FFT power until 21:23 when it crossed the poleward edge and recorded drops in VTEC of 10 TECU over 5 min and FFT power up to 0.06 TECU^2 Hz^{-1} and up to 0.2 Hz.

3.3. 21:30 to 22:50 UT, Entering the Midlatitude Trough

Near 21:30, the plume's poleward edge passed over the observation area, and PRNs 9, 16, 23, and 31 showed sudden increases in FFT power while near the plume's poleward edge—PRN 23 especially showed a large increase in FFT power >0.1 TECU^2 Hz^{-1} between 100 mHz and 300 mHz during 21:50–22:00 UT (Figure 4). During this interval, PRNs 7 (dark green), 9 (brown), and 16 (purple) were inside the low-density trough and also exhibited increased FFT power of ~0.03–0.05 TECU^2 Hz^{-1}. PRNs 19 and 27 were located entirely within the SED plume with no observable FFT power above 0.005 TECU^2 Hz^{-1}.

At 22:30 UT PRNs 7 and 9 were in the vicinity of a gradient between the trough and the trough minimum and, unlike the other PRN observed at this time, showed a small increase in FFT power >0.05 TECU^2 Hz^{-1} beginning at ~80 mHz and extending as high as 300 mHz. PRNs 16, 19, 23, and 27 were also within the trough—though either well inside the trough minimum or far away from its edge gradients and showed no increase in FFT power >0.005 TECU^2 Hz^{-1}.

3.4. 22:50 to 23:30, the Midlatitude Trough

Figure 5 shows the interval between 22:50 and 23:00 UT. Most of the observable PRN were located within the trough and away from density gradients near the SED plume or low-density trough minimum. VTEC values leveled off between 10 and 15 TECU and there were only minor changes in FFT power (~0.01 TECU^2 Hz^{-1})—mostly associated with PRNs 9 and 16, which were approaching the observed VTEC enhancement of the auroral oval. PRN 23 (light blue) was the closest to the SED plume and headed equatorward, though still lagging behind the SED plume's poleward edge. It recorded increasing VTEC as the plume's poleward gradient crossed over it, but no FFT power was observed above the noise floor. PRN 19 (black) traversed a similar portion of the plume during this time, but moving poleward, and showed a steady and smooth, but slightly steeper, decrease in density than PRN 23 away from the plume with no FFT power changes. PRNs 9 (brown) and 27 (blue) were near the trough region and showed a difference of ~2 TECU between the trough's poleward gradient (PRN 9) and its base (PRN 27), and their FFT spectra do not show any obvious small-scale variations. Meanwhile, PRN 7 (dark green) and PRN 16 (purple) were on the poleward edge of the trough, near the positive gradient into a region of auroral density enhancement. Both IPP time series showed low VTEC

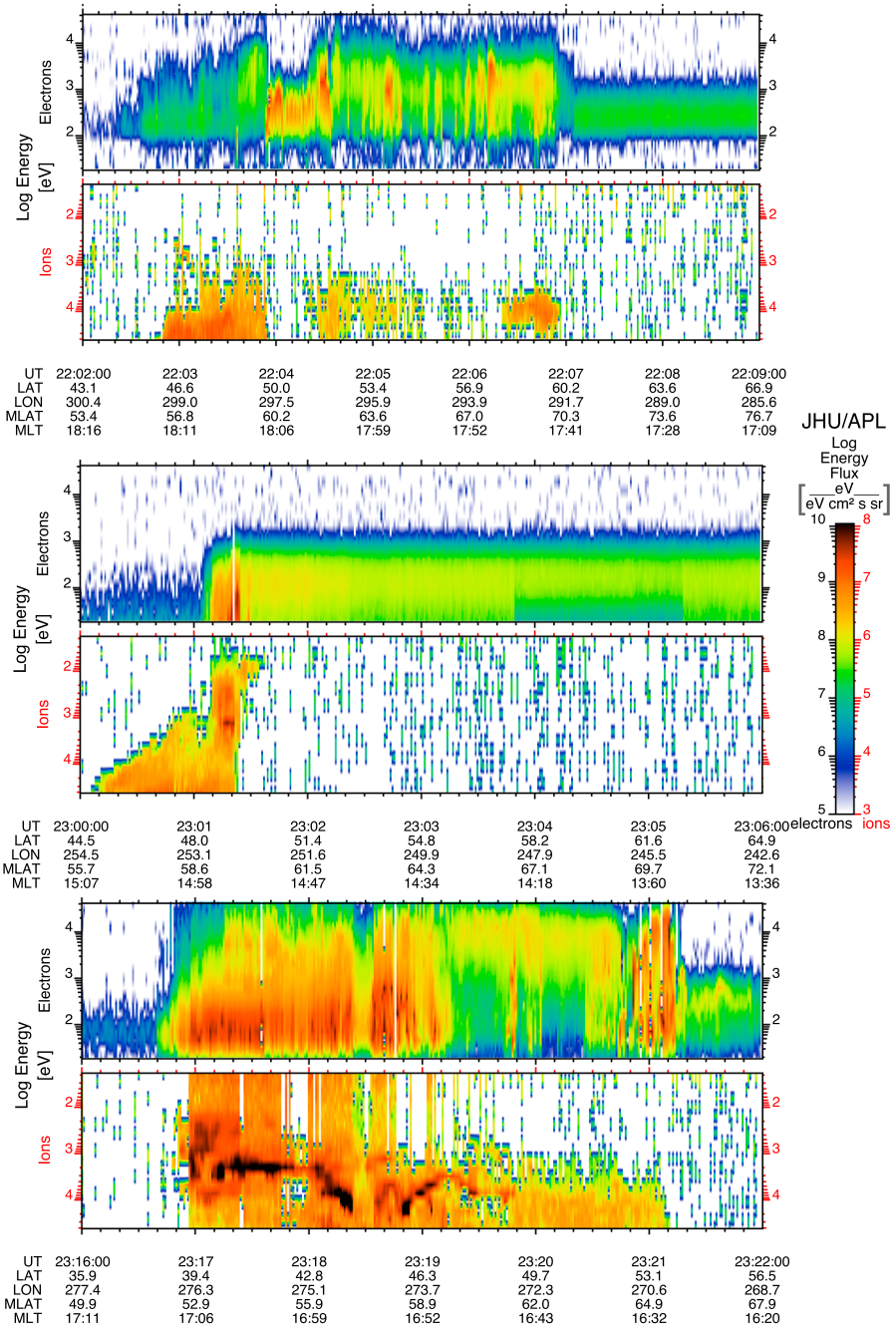

Figure 7. (top) DMSP F19 particle flux showing that auroral electron precipitation was 4° poleward of the SED plume within 18° east (1.2 h MLT) of the observation area. (middle) DMSP F16 showing auroral precipitation beginning >2° poleward of the SED plume within 15° west (1 h MLT) of the observation area. (bottom) DMSP F17 showing auroral precipitation beginning >2° poleward of the SED plume within the observation area consistent with TEC enhancement observed in this region at the time.

(10–15 TECU), with a slight increase of ~0.01 $TECU^2\ Hz^{-1}$ in the FFT power for PRN 7—likely due to small-scale structure in the auroral enhancement.

Figure 6 shows the interval between 23:10 and 23:20 UT. Shortly after the period shown in Figure 5, PRN 23 continued to track just poleward of the SED plume and showed a slight decrease in VTEC with some increased FFT power of 0.02 $TECU^2\ Hz^{-1}$ near 100 mHz. PRN 19, which had previously been parallel to PRN 23, continued its poleward track and traversed the low-density trough around 23:10 UT and measuring VTEC ~5 TECU

accompanied by FFT power of 0.03 $TECU^2$ Hz^{-1} at 100 mHz. PRNs 9, 16, and 27 continued to track poleward and crossed into the region of auroral enhancement and showed the expected increase in VTEC and strongly increased FFT power on a band at ~100 mHz and extending to 350 mHz (in the case of PRN 7). PRNs 7 and 30 (violet) traverse the edges of the densest regions of the auroral enhancement. They showed the expected increase in VTEC from auroral ionization and also a strong increase in FFT power (> 0.1 $TECU^2$ Hz^{-1}) centered around 100 mHz, and also broad increases to 200 mHz. Similar observations are made through 23:30 after which VTEC decreases for most PRN with amplitude fluctuations in FFT power < 0.02 $TECU^2$ Hz^{-1} near 100 mHz. During this time, PRN 11 (sea green) crossed the plumes poleward edge, but tracking northward from inside the plume it observed only slight increases in FFT power beginning near 100 mHz and extending to nearly 400 mHz. This is contrasted with earlier crossings of the plume's poleward edge that were closer to the tip of the plume and observed much higher FFT power.

3.5. Auroral Observations

Figure 7 shows DMSP particle flux intensity at 22:00, 23:00, and 23:20 UT measured near the observation region. At 22:00 UT DMSP satellite F19 observed increased proton and electron flux at 44.4°N, 299.8°E geodetic (52.4°N, 21.4°E CGM), suggesting the auroral boundary was poleward of the SED plume within 1 h of the Ann Arbor observation magnetic local time (MLT). AMPERE summary plots (not shown) also indicate upward radial current beginning at ~44–45°N geodetic latitude at Ann Arbor MLT, further suggesting that electron precipitation, and consequently the equatorward auroral boundary, began at least several degrees poleward of the SED plume's poleward edge. Similarly, at 23:00 and 23:17 UT, DMSP satellites F16 and F17 both observed increased precipitation fluxes beginning at least ~5° latitude poleward of the SED plume. Figure 6 shows the magnetic footprint track for DMSP F17 mapped to 300 km altitude as a white line with the enhanced particle flux shown from Figure 7 highlighted in pink beginning near ~41°N. The period of DMSP precipitation is spatially consistent with the enhanced TEC observed in both the single station TEC and MIT Madrigal TEC Maps.

4. Inference of Irregularity Size From Single Station GPS TEC Using Radar Velocities

During this same period, both Millstone Hill Incoherent Scatter Radar (ISR) and the SuperDARN radars at Christmas Valley East, Blackstone, Fort Hays East, and Wallops Island (e.g., Figure 1) show plasma velocities within the Ann Arbor observation area of ~1000 (±300) ms^{-1} in the *F* region. Assuming the irregularities are frozen-in with the bulk plasma flow, the increased spectral power observed in IPP crossings of the SED/trough and auroral/trough interfaces is consistent with what would be expected for irregularities between 3 km (±900 m) and 10 km (±3 km) in size transported past the IPPs at those velocities. The motion of the IPPs (50 ms^{-1}) is nearly stationary relative to the plasma flow and only slightly influences the observed frequency of FFT power (±10 mHz).

5. Discussion

During the passage of the SED plume on 17 March 2015 between 20:00 and 23:57 UT on 17 March 2015, several general trends are observed. First, there is little observed TEC variation indicated in the FFT spectra equatorward of the advancing SED plume, along its equatorward edge, or through the plume peak. The equatorward region is best illustrated by observations from PRNs 3 and 32, which do not cross the SED plume and travel ahead of the advancing equatorward edge of the plume throughout the observation, and show only occasional TEC variability—comparable with FFT spectra during quiet time conditions. This pattern is further reinforced by similar observations from PRN 16, as described in section 3.1, which also travels through the plume system's equatorward region, but crossing into the plume on a poleward trajectory and showed no FFT power above 0.005 $TECU^2$ Hz^{-1}. During the entire observation, seven PRNs pass through the SED plume and none exhibited FFT power above 0.005 $TECU^2$ Hz^{-1} prior to crossing the plume's poleward gradient. This suggests that small-scale irregularities are scarce equatorward of the SED plume and that the plume itself contains few kilometer-scale irregularities. Second, observations near the plume's poleward edge exhibit TEC variation and FFT power comparable to that observed in the aurora (~0.1 $TECU^2$ Hz^{-1})—consistent with the variability asymmetry between equatorward and poleward gradients reported by *Coster* [2007] and *Sun et al.* [2013]. As the PRN IPPs crossed the poleward edge of the SED plume and its boundary with the trough, sudden decreases in VTEC were accompanied by rapid fluctuations on multiple scales as indicated by the VTEC time series and FFT spectra, showing increased power up to 0.1 $TECU^2$ Hz^{-1} between 100 and 300 mHz. DMSP

and AMPERE observations confirm that this GPS TEC variability was not due co-located auroral irregularities. At both 22:00 and 23:00 UT, DMSP indicated vertical proton and electron fluxes beginning 4° poleward of the SED plume, and within 1 h MLT east and 2° latitude in the observation area. AMPERE field-aligned current (FAC) plots at 22:00 (not shown) also indicate downward FAC extending equatorward to ~44° geographic latitude while the SED plume's poleward edge was located at ~42°. Finally, as the trough/auroral boundary, an increase in VTEC variability and the FFT spectra showed increased power 0.05 to 0.1 $TECU^2$ Hz^{-1} around 100 mHz. This suggests the location of TEC gradients adjacent to the trough and colocated with high speed plasma flow.

In their recent paper, *Cherniak and Zakharenkova* [2015] suggest that irregularities observed in the polar cap may be transported from the midlatitude SED plume. The present observation and detection of small-scale irregularities associated with the SED plume support this suggestion. Furthermore, observations of longitudinal asymmetries in TEC structure between PRN with near-simultaneous crossings of the SED plume, such as those described in sections 3.2 and 3.4, demonstrate that the plume exhibits ~100 km scale longitudinal asymmetries in TEC variability observed at higher latitudes (45° to 50° latitude) not observed closer to the SED base region (35° to 40° latitude). This suggests that such structuring of the plume may be occurring as the plume moves toward the cusp and may be an early indicator of the formation of polar patches [*Zou et al.*, 2014].

6. Irregularity Altitude

Recent work by *Liu et al.* [2016] that characterized the density profile of the SED plume during 17 March 2015 SED plume suggests that the increased TEC observed in the SED plume may be due to density enhancements in the topside ionosphere and not n_mF_2. This is supported by Constellation Observing System for Meteorology, Ionosphere, and Climate (COSMIC) observations that saw a factor of 2 increase in topside TEC despite a decrease in n_mF_2. This suggests that irregularities during this storm may extend higher in altitude than the h_mF_2, consistent with *Coster et al.* [2003] and *Yuan et al.* [2009] which found that half of SED TEC is found above 800 km, *Moldwin et al.* [2016] which reviewed the body of literature connecting plasmaspheric and SED plumes, and *Yizengaw* [2005] which connected the plasmapause to the midlatitude trough.

Acknowledgments

This work was supported in part by grants from the National Science Foundation (AGS-1265651 and AGS-1342968) and the National Aeronautics and Space Administration (NNX14AF31G). This work was also made possible with data and support from the CEDAR Archival Madrigal Database at MIT Haystack Observatory; the Johns Hopkins Applied Physics Laboratory and the Defense Meteorological Satellite Program; the AMPERE team and the AMPERE Science Center; the National Oceanic and Atmospheric Administration; the Kyoto Disturbance Storm Time Index; the Blacksburg, Christmas Valley, Fort Hays, and Wallops Island SuperDARN radar sites; and the Virginia Tech SuperDARN repository. The authors would also like to acknowledge and thank the following individuals for review, discussion, and support: Philip Erickson, Yu (Jade) Morton, Anthea Coster, and Evan Thomas. University of Michigan GPS TEC Data products are available upon request (heinet@umich.edu). Madrigal TEC Map Data is available at http://madrigal.haystack.mit.edu/. SuperDARN Radar Data is available at http://vt.superdarn.org/. DMSP Data can be obtained using the DMSP Tool available at http://sd-www.jhuapl.edu/Aurora/data/app/DMSP.jnlp.

7. Conclusion

Combining temporal and frequency analysis from single GPS ground receivers has been used to suggest the presence of ionospheric irregularities in various regions of the SED plume/trough/auroral system as indicated on TEC maps and in the time series data of single station GPS TEC time series. The addition of radar observations to these analyses provides an estimate between 3 and 10 km for the length scale of irregularities primarily located on the SED plume's poleward edge, but also observed in the trough during the 17 March 2015 storm. However, this length scale range is limited by the observation sample rate at 1 Hz and smaller irregularities may also be present. Future work will investigate additional storms, expand the range of detectable frequencies with TEC sample rates up to 20 Hz, and incorporate additional high-rate TEC stations now coming online.

References

Basu, S., and K. M. Groves (2001), Specification and Forecasting of Outages on Satellite Communication and Navigation Systems, in *Space Weather*, edited by S. Basu and K. M. Groves, pp. 423–430, AGU, Washington, D. C.

Basu, S., et al. (2008), Large magnetic storm-induced nighttime ionospheric flows at midlatitudes and their impacts on GPS-based navigation systems, *J. Geophys. Res.*, *113*, A00A06, doi:10.1029/2008JA013076.

Bramley, E. N., and R. Browning (1978), Mid-latitude ionospheric scintillation of geostationary satellite signals at 137 MHz, *J. Atmos. Terr. Phys.*, *40*(12), 1247–1255, doi:10.1016/0021-9169(78)90075-2.

Cherniak, I., and I. Zakharenkova (2015), Dependence of the high-latitude plasma irregularities on the auroral activity indices: A case study of 17 March 2015 geomagnetic storm, *Earth Planets Space*, *67*(1), 151, doi:10.1186/s40623-015-0316-x.

Coster, A., J. Foster, and P. Erickson (2003), Monitoring the ionosphere with GPS, *GPS World*, *14*(5), 42–49.

Coster, A. J. (2007), Mitigation of ionospheric propagation errors with GPS, in *2007 IEEE Radar Conference*, pp. 922–926, IEEE, Waltham, Mass., doi:10.1109/RADAR.2007.374342.

Datta-Barua, S., P. H. Doherty, S. H. Delay, T. Dehel, and J. A. Klobuchar (2003), Ionospheric scintillation effects on single and dual frequency GPS positioning, in *Proceedings of ION GPS/GNSS*, pp. 336–346, Inst. of Navig., Portland, Oreg.

Datta-Barua, S., T. Walter, G. S. Bust, and W. Wanner (2014), Effects of solar cycle 24 activity on WAAS navigation, *Space Weather*, *12*, 46–63, doi:10.1002/2013SW000982.

Doherty, P., A. J. Coster, and W. Murtagh (2004), Space weather effects of October-November 2003, *GPS Solutions*, *8*(4), 267–271, doi:10.1007/s10291-004-0109-3.

Foster, J. C. (1993), Storm time plasma transport at middle and high latitudes, *J. Geophys. Res.*, *98*(A2), 1675–1689, doi:10.1029/92JA02032.

Foster, J. C., and W. J. Burke (2002), SAPS: A new categorization for sub-auroral electric fields, *Eos Trans. AGU*, *83*(36), 393–394, doi:10.1029/2002EO000289.

Foster, J. C., and W. Rideout (2005), Midlatitude TEC enhancements during the October 2003 superstorm, *Geophys. Res. Lett.*, *32*, L12S04, doi:10.1029/2004GL021719.

Hargreaves, J. K. (1992), *The Solar-Terrestrial Environment an Introduction to Geospace—The Science of the Terrestrial Upper Atmosphere, Ionosphere, and Magnetosphere*, Cambridge Univ. Press, Cambridge, U. K., and New York.

Kelley, M. C., M. N. Vlasov, J. C. Foster, and A. J. Coster (2004), A quantitative explanation for the phenomenon known as storm-enhanced density, *Geophys. Res. Lett.*, *31*, L19809, doi:10.1029/2004GL020875.

Ledvina, B. M., J. J. Makela, and P. M. Kintner (2002), First observations of intense GPS L1 amplitude scintillations at midlatitude, *Geophys. Res. Lett.*, *29*, 1659, doi:10.1029/2002GL014770.

Liu, J., W. Wang, A. Burns, X. Yue, S. Zhang, Y. Zhang, and C. Huang (2016), Profiles of ionospheric storm-enhanced density during the 17 March 2015 great storm: SED DURING A GREAT STORM, *J. Geophys. Res. Space Physics*, *121*, 727–744, doi:10.1002/2015JA021832.

Moldwin, M. B., S. Zou, and T. Heine (2016), The story of plumes: The development of a new conceptual framework for understanding magnetosphere and ionosphere coupling, *Ann. Geophys.*, *34*(12), 1243–1253, doi:10.5194/angeo-34-1243-2016.

Pi, X., A. J. Mannucci, U. J. Lindqwister, and C. M. Ho (1997), Monitoring of global ionospheric irregularities using the worldwide GPS network, *Geophys. Res. Lett.*, *24*(18), 2283–2286, doi:10.1029/97GL02273.

Schunk, R., and A. Nagy (2009), *Ionospheres: Physics, Plasma Physics, and Chemistry*, Cambridge Univ. Press, Cambridge, U. K.

Seo, J., T. Walter, and P. Enge (2011), Correlation of GPS signal fades due to ionospheric scintillation for aviation applications, *Adv. Space Res.*, *47*(10), 1777–1788, doi:10.1016/j.asr.2010.07.014.

Simon, A. (1963), Instability of a partially ionized plasma in crossed electric and magnetic fields, *Phys. Fluids*, *6*(3), 382–388, doi:10.1063/1.1706743.

Sun, Y.-Y., T. Matsuo, E. A. Araujo-Pradere, and J.-Y. Liu (2013), Ground-based GPS observation of SED-associated irregularities over CONUS, *J. Geophys. Res. Space Physics*, *118*, 2478–2489, doi:10.1029/2012JA018103.

van der Meeren, C., K. Oksavik, D. Lorentzen, J. I. Moen, and V. Romano (2014), GPS scintillation and irregularities at the front of an ionization tongue in the nightside polar ionosphere, *J. Geophys. Res. Space Physics*, *119*, 8624–8636, doi:10.1002/2014JA020114.

Yeh, K. C., and C.-H. Liu (1982), Radio wave scintillations in the ionosphere, *Proc. IEEE*, *70*(4), 324–360.

Yizengaw, E. (2005), The altitude extension of the mid-latitude trough and its correlation with plasmapause position, *Geophys. Res. Lett.*, *32*, L09105, doi:10.1029/2005GL022854.

Yuan, Z.-G., X.-H. Deng, S.-R. Zhang, W.-X. Wan, and B. W. Reinisch (2009), F region behavior in the SED plume during a geomagnetic superstorm: A case study, *J. Geophys. Res.*, *114*, A08303, doi:10.1029/2008JA013841.

Zou, S., A. J. Ridley, M. B. Moldwin, M. J. Nicolls, A. J. Coster, E. G. Thomas, and J. M. Ruohoniemi (2013), Multi-instrument observations of SED during 24–25 October 2011 storm: Implications for SED formation processes, *J. Geophys. Res. Space Physics*, *118*, 7798–7809, doi:10.1002/2013JA018860.

Zou, S., M. B. Moldwin, A. J. Ridley, M. J. Nicolls, A. J. Coster, E. G. Thomas, and J. M. Ruohoniemi (2014), On the generation/decay of the Storm-Enhanced Density (SED) plumes: Role of the convection flow and field-aligned ion flow, *J. Geophys. Res. Space Physics*, *119*, 543–8559, doi:10.1002/2014JA020408.